

1 Revision 1

2 Word count: 7853

3 **Thermal equation of state of Fe₃O₄ magnetite up to 16 GPa and 1100 K**

4 Nicki C. Siersch^{1,*}, Giacomo Criniti², Alexander Kurnosov², Konstantin Glazyrin³, Daniele
5 Antonangeli¹

6 ¹ Sorbonne Université, Muséum National d'Histoire Naturelle, UMR CNRS 7590, Institut de
7 Minéralogie, de Physique des Matériaux et de Cosmochimie, IMPMC, Paris, France.

8 ² Bayerisches Geoinstitut, Universität Bayreuth, D-95440 Bayreuth, Germany.

9 ³ Deutsches Elektronen-Synchrotron DESY, Notkestr. 85, D-22607 Hamburg, Germany.

10 * Corresponding author: nsiersch@gmail.com

11

12 nsiersch@gmail.com

13 giacomo.criniti@uni-bayreuth.de

14 alexander.kurnosov@uni-bayreuth.de

15 konstantin.glazyrin@desy.de

16 daniele.antonangeli@upmc.fr

17

18

Abstract

19 Fe₃O₄ magnetite is an important mineral commonly found in various geological settings,
20 including the planet Mars, whose thermo-elastic properties at high pressure and temperature
21 are still poorly constrained. We performed X-ray diffraction measurements on natural

22 magnetite using resistive-heated diamond anvil cells up to 16 GPa and 1100 K. We fitted a
23 thermal equation of state (EoS) to the collected data resulting in $K_0 = 182(1)$ GPa, $K'_0 = 4$, θ_D
24 $= 660$ K, $\gamma = 1.8(1)$, and $q = 2.7$. Moreover, it was possible to explore the structural evolution
25 of magnetite in detail using single-crystal measurements. Over the studied pressure and
26 temperature range, we found no evidence of a transformation from an inverse to a normal
27 spinel structure. The EoS parameters obtained in this study will allow to be implemented into
28 currently available databases for self-consistent thermodynamic modeling. In particular, the
29 obtained results are used to model and compare the sound wave velocities of a magnetite-
30 bearing and magnetite-free Martian upper mantle assemblage. We observe that the
31 incorporation of magnetite reduces the sound wave velocities, however, the magnitude of the
32 effect is below the current seismic detection limit of the InSight mission on Mars at the low
33 abundance of magnetite expected in the Martian mantle.

34

35 **Keywords:** magnetite, thermal equation of state, X-ray diffraction, high-pressure, high-
36 temperature

37

38

Introduction

39 Magnetite (α -Fe₃O₄) is an important mineral commonly found in igneous, sedimentary and
40 metamorphic rocks of the Earth and in meteorites, which also finds industrial applications,
41 going from being a traditional recording medium to the emerging field of spin electronics.
42 Magnetite was also recently suggested to be potentially stable in the most oxidized regions of
43 the upper mantle of Mars (Xu et al. 2021). Magnetite crystallizes at ambient pressure in a
44 cubic structure above the Verwey temperature of $T_V \sim 120$ K (Verwey 1939), in the space
45 group $Fd\bar{3}m$ with $Z = 8$. It has an inverse spinel structure with the tetrahedrally-coordinated

46 sites being fully occupied by Fe^{3+} , whereas the remaining Fe^{2+} and Fe^{3+} are randomly
47 distributed between the octahedrally-coordinated sites ($[\text{Fe}^{3+}]_{\text{T}}[\text{Fe}^{2+}\text{Fe}^{3+}]_{\text{O}}\text{O}_4$). This is in
48 contrast to a normal spinel structure where the tetrahedrally-coordinated sites are occupied by
49 the divalent cation and the octahedrally-coordinated sites are filled with the trivalent cation.
50 With increasing pressure, magnetite was found to undergo a gradual phase transformation to
51 the so-called h- Fe_3O_4 (Mao et al. 1974; Huang and Bassett 1986; Fei et al. 1999; Haavik et al.
52 2000; Lazor et al. 2004) or, following a newer nomenclature, $\beta\text{-Fe}_3\text{O}_4$ (Khandarkhaeva et al.
53 2022). Mao et al. (1974) were the first to report the transformation from magnetite to $\beta\text{-Fe}_3\text{O}_4$
54 above 25 GPa as observed by powder X-ray diffraction in a diamond anvil cell (DAC). The
55 transformation was described to be sluggish, especially at ambient temperature, with the
56 completion of the phase transformation being faster at 600 K. These findings were confirmed
57 by the study of Huang and Bassett (1986), which reported a large two-phase hysteresis upon
58 compression and decompression. The structure of $\beta\text{-Fe}_3\text{O}_4$ was initially suggested to be
59 monoclinic (Mao et al. 1974), but subsequent Rietveld refinements performed on powdered
60 magnetite in a resistively-heated DAC proposed $\beta\text{-Fe}_3\text{O}_4$ to have the orthorhombic CaMn_2O_4 -
61 type structure in the space group *Pbcm* (Fei et al. 1999). A more recent study by Haavik et al.
62 (2000) confirmed $\beta\text{-Fe}_3\text{O}_4$ to be orthorhombic, but having the CaTi_2O_4 -type structure in the
63 space group *Cmcm*. This structure was further confirmed by Lazor et al. (2004) who also
64 performed Rietveld refinements on polycrystalline magnetite and a recent study by
65 Khandarkhaeva et al. (2022), who performed single-crystal X-ray diffraction experiments in
66 laser-heated DACs. The latter also reported two new Fe_3O_4 polymorphs, namely $\gamma\text{-Fe}_3\text{O}_4$
67 having the Yb_3S_4 -type structure in space group *Pnma* stable at 64-73 GPa upon heating at
68 1500-2000 K, and $\delta\text{-Fe}_3\text{O}_4$ having the Th_3P_4 -type structure in space group $\bar{I}42d$ stable at 78(1)
69 GPa and 4800(300) K (Khandarkhaeva et al. 2022).

70 In the stability field of α -Fe₃O₄ at pressures below the structural transformation into β -Fe₃O₄,
71 the material retains the cubic structure. However, within this pressure range, the electronic
72 state of magnetite is quite controversial. Several studies using Mössbauer spectroscopy and
73 powder X-ray diffraction introduced the notion of a possible coordination crossover in the
74 magnetite structure, with the electronic charge density shifting from the octahedral to
75 tetrahedral sites, hence inducing an inverse to normal spinel transition (Pasternak et al. 2003;
76 Rozenberg et al. 2007). Above 7 GPa, magnetite is suggested to first transform from an
77 inverse spinel to an intermediate state, and then to a normal spinel above 17 GPa at 300 K
78 (Pasternak et al. 2003; Rozenberg et al. 2007). The same process was observed with
79 decreasing temperature (Pasternak et al. 2003). A more recent investigation by single-crystal
80 XRD and Mössbauer spectroscopy (Glazyrin et al. 2012), however, could not confirm these
81 observations and the proposed scenario, at least up to a pressure of 25 GPa at 300 K. An
82 additional magnetic transition was proposed by Ding et al. (2008) who, based on Fe K-edge
83 X-ray magnetic circular dichroism measurements, suggested a high-spin to intermediate-spin
84 transition of the Fe²⁺ ions between 12 and 16 GPa that, noteworthy, is incompatible with an
85 inverse to normal spinel transition as described by Pasternak et al. (2003) and Rozenberg et al.
86 (2007). Glazyrin et al. (2012) found the volume change associated to such a transition too
87 small to be resolved with single-crystal XRD, and further found no evidence for a spin
88 transition in their Mössbauer spectroscopy data. Additional investigations are needed to
89 confirm the existence and clarify the nature of these pressure- and/or temperature-induced
90 modifications affecting either electronic or magnetic degrees of freedom, also as a function of
91 different pressure media and the effects of non-hydrostatic conditions.

92 Recently, experimental studies confirmed the presence of magnetite next to majoritic garnet in
93 Earth's mantle assemblages (Tao et al. 2018) and in equilibrium with pyroxene and olivine in
94 upper mantle assemblages representative for Mars (Xu et al. 2021) making it even more

95 relevant to investigate the thermo-elastic properties of magnetite. Until now, the elastic
96 properties of magnetite have been determined only at room temperature using a large number
97 of different techniques including powder X-ray diffraction (e.g. Mao et al. 1974; Haavik et al.
98 2000 and references therein; Lazor et al. 2004; Rozenberg et al. 2007), single-crystal X-ray
99 diffraction (e.g. Finger et al. 1986; Nakagiri et al. 1986; Kuriki et al. 2002; Reichmann and
100 Jacobsen 2004; Gatta et al. 2007; Glazyrin et al. 2012) and ultrasonic interferometry (e.g.
101 Reichmann and Jacobsen 2004). The bulk modulus K_0 obtained in the above-mentioned
102 studies fall in a large range between 141 and 222 GPa, with its pressure derivative K'_0 ranging
103 between 3.6 and 7.5. Once limiting to studies performed after the year 2000, predominantly
104 conducted using single-crystal XRD (Reichmann and Jacobsen 2004; Gatta et al. 2007;
105 Glazyrin et al. 2012) and powder XRD (Rozenberg et al. 2007), results are more comparable,
106 with K_0 between 180 and 189 GPa and K'_0 in the range 3.6 to 5.2. Until now, only one study
107 (Lazor et al. 2004) attempted to determine the compressibility of magnetite at high
108 temperatures, without reporting the actual data. The thermo-elastic properties of magnetite,
109 however, are critically needed, for example to be able to model density and wave velocities
110 through a magnetite-bearing phase assemblage, e.g. representing the Martian upper mantle
111 (Xu et al. 2021).

112 The aim of this study is two-fold: 1) to determine the thermal equation of state of Fe_3O_4
113 magnetite up to 16 GPa and 1100 K using X-ray diffraction combined with resistive-heated
114 diamond anvil cells and 2) to investigate the structural evolution of magnetite in order to
115 elucidate any structural changes leading towards a phase transformation at high pressure and
116 temperature.

117

118

Methods

119 A natural magnetite sample grown on a mica schist bedrock sourced from Chester, Vermont,
120 USA has been used as starting material for all powder and single-crystal measurements at
121 high pressure and high temperature. The electron microprobe, operated at 15 keV and 10 nA
122 with a focused beam, was calibrated using diopside as standard for Mg, Si and Ca, albite for
123 Na, orthoclase for Al, Fe₂O₃ for Fe, Cr₂O₃ for Cr, and used to obtain the chemical
124 composition of the natural magnetite. Analyses on 60 individual spots on a one-sided polished
125 magnetite sample embedded in epoxy resulted in the chemical composition reported in Table
126 1, confirming the high purity of this natural magnetite sample. This natural sample is purer
127 (99.5%) in comparison to the natural magnetite sample investigated by Glazyrin et al. (2012)
128 having a purity of 99.2%. The sample was crushed dry in an agate mortar for 30 min until a
129 fine-grained homogeneous powder was obtained.

130 High pressure and high temperature experiments were prepared and performed at the Extreme
131 Conditions Beamline P02.2 of PETRA III (Hamburg, Germany) (Liermann et al. 2015). Two
132 Mao-type symmetric DACs were prepared and dedicated to XRD measurements at high-
133 pressure and ambient temperature on a single-crystal (run hereafter referred to as
134 DAC_300Ksc) and on a powdered sample (DAC_300Kpwd), respectively. DAC_300Ksc was
135 equipped with two Boehler-Almax diamonds (Boehler and De Hantsetters 2004) having a
136 culet diameter of 400 μm . A 200 μm thick Re gasket was indented to 73 μm and a hole of 200
137 μm diameter was laser-drilled in the center of the indentation acting as sample chamber. A
138 single-crystal of around 40x60x20 μm^3 was placed in the center of the culet next to a small
139 ruby sphere acting as a fluorescence pressure gauge (Dewaele et al. 2004). DAC_300Kpwd
140 was prepared with standard diamonds of 400 μm culet diameter. The Re gasket was prepared
141 in the same way as described above. The powdered pelleted sample was placed inside the
142 sample chamber together with a ruby sphere. Both DACs were gas-loaded with neon acting as
143 quasi-hydrostatic pressure transmitting medium (Liermann et al. 2015) as it was reported to

144 provide conditions as hydrostatic as helium gas up to at least 19 GPa at ambient temperature
145 (Scheidl et al. 2016). During all experiments the pressure was increased remotely using a gas-
146 driven membrane.

147 Three resistively-heated DACs (DAC_600K, DAC_900K and DAC_1100K) were prepared
148 with one standard (upstream) and one Boehler-Almax diamond (downstream) each,
149 employing diamonds of 300 μm culet for DAC_600K and DAC_900K and of 400 μm culet
150 for DAC_1100K. A couple of 0.5 mm thick graphite heaters connected by two Mo electrodes
151 built inside the DACs allowed generating stable high temperatures (designed after Lawrence
152 Livermore 4-pin cells). Heaters from layered graphite surrounding the Re gasket are forming
153 a homogenous heating field at the diamond tips and temperatures up to 1100 K inside the
154 sample chamber. Re gaskets were pre-indented to a thickness of $\sim 40\text{-}70$ μm and sample
155 chambers of 130-150 μm in diameter were drilled. The temperature was monitored using two
156 individual R-type thermocouples per DAC, positioned as close to the sample chamber as
157 possible. The average of the two readings was assumed as the sample's temperature and the
158 standard deviation was taken as uncertainty (Table 2). DAC_600K was loaded with a single-
159 crystal magnetite sample and $\text{SrB}_4\text{O}_7\text{:Sm}^{2+}$ acting as pressure gauge throughout the
160 experiment (Rashchenko et al. 2015). DAC_900K and DAC_1100K were loaded with a
161 powdered and single-crystal magnetite sample, respectively, together with gold nano-powder
162 for pressure determination (Dorogokupets and Dewaele 2007). For DAC_1100K fitting of 1D
163 patterns was preferred at high pressure and temperature above 900 K because the quality of
164 the single-crystal data was not ideal anymore. All three DACs were loaded with silicon oil as
165 pressure transmitting medium, which provides a good compromise between hydrostaticity and
166 risk of diamond failure events. Our experiment at 600 K confirmed the efficiency of silicon
167 oil as quasi-hydrostatic pressure medium at high temperatures. The membrane-driven

168 resistively-heated DACs were placed into a vacuum chamber, to avoid oxidation at high
169 temperatures of graphite heaters, cell components and diamonds.

170 Reference values for the unit cell volumes of magnetite (both powder and single-crystal) and
171 gold nano-powder, were measured at ambient conditions prior to the compression
172 experiments, as well as the fluorescence lines of ruby and SrB₄O₇:Sm²⁺. In this procedure,
173 both the magnetite samples and the pressure standards were measured being placed inside the
174 sample chamber of a DAC without any pressure transmitting medium. By employing an X-
175 ray beam having a focused spot size of 8(H) x 3(V) μm² full width at half maximum (FWHM)
176 at 25.6 keV, diffraction patterns of magnetite and gold nano-powder were recorded using a
177 Perkin-Elmer XRD 1621 flat panel detector (Liermann et al. 2015). Polycrystalline CeO₂ and
178 a single-crystal of natural enstatite (Mg_{1.93}Fe_{0.06}Si_{1.93}Al_{0.06}O₆, *Pbca*; *a*=18.2391(3) Å;
179 *b*=8.8117(2) Å; *c*=5.18320(10) Å) were used to calibrate the sample to detector distance and
180 the detector parameters for powder and single-crystal diffraction. Single-crystal diffraction
181 data at high pressure were collected upon continuous rotation of samples around a vertical
182 axis (ω) between ±30° in steps of 0.5°. The acquisition time of each frame was 0.5 s/frame
183 and a Pt absorber of 50 μm was used to avoid saturating the detector. Diffraction data used for
184 precise lattice parameter determination from integrated 1D profiles were collected upon
185 rotation of the DAC between ±20° in ω with an exposure time of 20 s and using a Pt absorber
186 of 50 μm.

187 For the high-temperature runs, the samples were pre-compressed to a low starting pressure,
188 within the silicon oil field of quasi-hydrostaticity. Then the temperature was increased to the
189 target value and left to stabilize for half an hour. XRD patterns were collected upon
190 compression every 1 to 2 GPa at a constant temperature up to ~14 GPa. For DAC_1100K,
191 XRD patterns were collected every 100 K starting from 600 K while increasing to the target
192 temperature of 1100 K. The collected diffraction data were integrated using DIOPTAS

193 (Prescher and Prakapenka 2015) and analyzed using full profile LeBail refinements with the
194 GSAS software package in the EXPGUI interface (Toby 2001; Larson and Von Dreele 2004).
195 Processing of single-crystal diffraction data, which included orientation determination,
196 indexing, intensity integration, correction for Lorentz and polarization factors, and empirical
197 absorption correction based on spherical harmonics (ABSPACK), was carried out using
198 *CrysAlisPro* 1.0.43 (Rigaku, Oxford Diffraction).

199 Structural refinements were performed for data collected in DAC_300Ksc, DAC_600K and
200 for the first four points of DAC_1100K using the ShelXle software (Hübschle et al. 2011;
201 Sheldrick 2015). Isotropic displacement parameters were used to reduce the number of refined
202 parameters due to the limited number of reflections at high pressure and temperature in the
203 DAC. Between 26 and 38 unique reflections could be used, depending on pressure and
204 temperature to refine 5 individual parameters. Details of the structural refinements are
205 reported in the deposited CIF and in Table S1.

206

207

Results and Discussion

208 *P-V-T* equation of state of Fe₃O₄ magnetite

209 The variation with pressure of the unit-cell volumes of magnetite at ambient temperature
210 collected on a single-crystal and a powdered sample in two separate runs, normalized with
211 respect to their room pressure values, shows a smooth decrease up 15.7 GPa, the highest
212 pressure reached in this study (Figure 1a). Plotting the normalized stress F_E versus Eulerian
213 finite strain f_E (Figure S1) shows a horizontal line over the entire pressure range. Therefore, a
214 second-order Birch-Murnaghan equation of state (BM2 EoS) can be applied to fit the
215 combined *P-V* data, normalized to the corresponding V_0 , as implemented in the EoSfit7 GUI
216 software (Angel et al. 2014; Gonzalez-Platas et al. 2016), resulting in an isothermal bulk

217 modulus $K_{T0} = 184(1)$ GPa with its pressure derivative K'_{T0} fixed to 4. Fit to a third-order BM
218 EoS (BM3 EoS) gives comparable results, with $K_{T0} = 181(3)$ GPa and $K'_{T0} = 4.6(5)$. Fitting
219 the two datasets individually with BM2 EoS results in values of K_{T0} of 183(1) GPa and 184(1)
220 for powder and single-crystal data, respectively, thus, within mutual uncertainties. The unit-
221 cell volumes reported by several studies (Finger et al. 1986; Nakagiri et al. 1986; Kuriki et al.
222 2002; Reichmann and Jacobsen 2004; Gatta et al. 2007; Rozenberg et al. 2007; Glazyrin et al.
223 2012) are in very good agreement with the P - V data collected in this study (Figure 1a). We
224 note that all these studies, except for Rozenberg et al. (2007), were performed on synthetic or
225 natural single-crystals and using quasi-hydrostatic pressure transmitting media such as a 4:1
226 methanol:ethanol mix for measurements below 4.5 GPa (Finger et al. 1986; Nakagiri et al.
227 1986), 16:3:1 methanol:ethanol:water below 9 GPa (Reichmann and Jacobsen 2004; Gatta et
228 al. 2007) or neon up to 21 GPa (Glazyrin et al. 2012). The P - V data reported by Rozenberg et
229 al. (2007) is the only study performed on powdered magnetite that is in agreement with our
230 study, most likely because their data have been collected using helium as pressure
231 transmitting medium, so under hydrostatic conditions. Four further studies by Mao et al.
232 (1974), Haavik et al. (2000), Kuriki et al. (2002) and Lazor et al. (2004) show a stiffer
233 compression behavior, especially at pressures above ~ 10 GPa (Figure 1a). Three out of the
234 four X-ray diffraction studies have been performed on powders in DACs, with the exception
235 of Kuriki et al. (2002), who performed measurements on a single-crystal. Employed pressure-
236 transmitting media, namely N_2 (Haavik et al. 2000), NaCl (Mao et al. 1974; Lazor et al. 2004)
237 and a methanol:ethanol mixture (Kuriki et al. 2002) are known to have low hydrostatic limits
238 of 3-10.5 GPa (N_2 and NaCl, e.g. Angel et al. 2007; Klotz et al. 2009) and <4 GPa
239 (methanol:ethanol, e.g. Piermarini et al. 1973; Otto et al. 1998). The stiffer compressibility
240 reported in these studies might therefore arise from non-hydrostatic stresses developed upon
241 compression, in particular at the highest pressures of the data collection. The observed
242 behavior could also be explained by the effect of deviatoric stress resulting in ‘pressure

243 overestimation' when, although the sample volume is measured correctly, the corresponding
244 pressure is systematically biased, e.g. due to a different stress on a pressure sensor (Glazyrin
245 et al. 2016).

246 The unit-cell volumes of magnetite collected in this study along four isotherms, at 300 K,
247 600(50) K, 869(57) K and 1068(72) K, are reported in Table 2 and illustrated in Figure 1b.
248 The expected increase of the unit-cell volume with increasing temperature is well visible. The
249 single-crystal and powder data (represented by open and closed circles, respectively) collected
250 up to 1070 K (DAC_1100K) every 100 K starting from 600 K are in good agreement with the
251 volumes collected in the runs DAC_600K and DAC_900K within uncertainties. The entire P -
252 V - T dataset was fitted by a BM2 EoS combined with a Mie-Grüneisen-Debye (MGD) model
253 for the thermal pressure, using the EoSfit7 GUI software (Angel et al. 2014; Gonzalez-Platas
254 et al. 2016) to obtain V_0 and K_{T0} and the high-temperature parameters, namely the Debye
255 temperature θ_D , the Grüneisen parameter γ and its logarithmic volume derivative q . We took
256 advantage of the q -compromise Mie-Grüneisen-Debye approach implemented in EoSfit7 GUI
257 (Angel et al. 2020) in order to reduce the number of fitting parameters and the otherwise large
258 correlation of q with γ in the relatively limited pressure and temperature range targeted in this
259 study. Still, refining K_0 , θ_D , and γ was yielding larger correlations and thus uncertainties,
260 especially for θ_D and γ ($\theta_D = 1397(865)$ K with $V_0 = 44.604(7)$ cm³/mol, $K_0 = 182(1)$ GPa and
261 $\gamma = 2.3(8)$). The value of θ_D was therefore fixed to 660 K (Kouvel 1956) which is also in
262 agreement with the Debye temperature calculated for an Fe oxide having a mean atomic mass
263 of ~ 29 (Stixrude and Lithgow-Bertelloni 2011). The final fitting results are $V_0 = 44.603(7)$
264 cm³/mol, $K_0 = 182(1)$ GPa and $\gamma = 1.8(1)$ (solid lines in Figure 1b). In order to test the
265 influence of q on γ , the fitting procedure was repeated with q fixed to 2.7, the value proposed
266 by Stixrude and Lithgow-Bertelloni (2005, 2011) for the two spinels reported in their

267 database, namely the spinels MgAl_2O_4 and FeAl_2O_4 . The resulting fitting parameters were
268 exactly the same as the results obtained from the q -compromise approach reported above.

269

270 **Structural evolution of Fe_3O_4 magnetite at high pressure and high temperature**

271 Single-crystal data collected along the two isotherms at 300 K and 600 K and four additional
272 points obtained while increasing the temperature in the DAC to 1100 K have been used to
273 refine the structure of magnetite at high pressure and temperature. Figure 2a shows the
274 evolution of the polyhedral volumes, namely the octahedral and tetrahedral volumes, with
275 increasing pressure at room temperature. Both data sets at 300 K were fit to a BM2 EOS
276 resulting in bulk moduli $K_{0,tet}$ and $K_{0,oct}$ of 210(13) and 169(4) GPa, respectively. The
277 compressibility of the tetrahedra is therefore smaller compared to compressibility of the
278 octahedra. The here-measured compressibilities are in agreement with the values expected
279 according to a model based on ionic potential ($\text{IP}=\text{valence state}/\text{ionic radius}$) proposed by
280 Bruschini et al. (2015), namely $K_{0,tet}$ and $K_{0,oct}$ of 230 and 180 GPa, respectively. Our
281 measurements thus support the validity of this relatively simple model for predicting the bulk
282 moduli for spinel compositions. Figure 2a also compares the evolution of polyhedral volumes
283 with pressure to literature data obtained from single-crystal (Finger et al. 1986; Gatta et al.
284 2007; Glazyrin et al. 2012) or powder XRD (Haavik et al. 2000; Rozenberg et al. 2007). The
285 data collected in this study are in good agreement with the data reported by Glazyrin et al.
286 (2012). The compressibility data by Gatta et al. (2007) shows slightly softer tetrahedral and
287 stiffer octahedral volumes, respectively. Single-crystal data by Finger et al. (1986) are in very
288 good agreement with the tetrahedral volumes reported in this study, whereas a stronger
289 decrease with pressure for the octahedral volumes were observed. The compressibility of the
290 tetrahedral site measured by Haavik et al. (2000) is in good agreement until ~ 16 GPa, but
291 then becomes stiffer. The octahedral volumes already start deviating to a stiffer behavior

292 above ~10 GPa. This directly reflects the stiffer behavior of the unit-cell volume above 10
293 GPa (Figure 1a), likely due to non-hydrostatic stresses in their DAC experiment (Haavik et al.
294 2000). The pronounced decrease and increase for octahedral and tetrahedral volumes starting
295 from ~7 GPa reported by Rozenberg et al. (2007), which was ascribed to the onset of an
296 inverse to normal spinel transition, is not supported by the present data set. However, as the
297 pronounced changes reported by Rozenberg et al. (2007) are exactly opposite for tetrahedral
298 and octahedral volumes inside the magnetite structure, the mean compressibility of the unit-
299 cell volume is not influenced, resulting in the good agreement with the unit-cell volumes
300 reported in this study (Figure 1a).

301 Figure 2b shows the polyhedral volumes versus pressure along the two isotherms measured in
302 this study. As expected, the polyhedral volumes are slightly larger at high temperatures
303 (Figure 2b), while temperature-induced softening is not clearly visible. No abrupt change in
304 polyhedral volumes can be observed that could be linked to a phase transformation or a
305 distinct structural change in magnetite. Furthermore, we performed a test on our structural
306 refinement data allowing the site occupancy factor of Fe in octahedral coordination to be
307 refined. Results show no evidence of a transformation to maghemite ($\text{Fe}^{3+}_{0.67}\square_{0.33}\text{Fe}^{3+}_2\text{O}_4$)
308 upon heating, arguing against the possible oxidation of our samples during the high-
309 temperature experiments.

310 The evolution of the oxygen coordinate u , controlling the individual volumes of tetrahedra
311 and octahedra, was used by Rozenberg et al. (2007) to support their hypothesis of the onset of
312 inverse to normal spinel transition. In Figure 3, we report the oxygen coordinate u versus
313 pressure at 300 K, and the high-temperature single-crystal data collected in this study. The
314 data points show an almost constant trend, with only a slight increase with pressure. We also
315 note that, within uncertainties, the values of u are very similar for ambient temperature as well
316 as for the high temperature datasets. This provides evidence that no normal spinel component

317 appears upon heating in our samples. Our data are in good agreement with values reported in
318 literature, which however generally have a larger scatter and larger uncertainties (Finger et al.
319 1986; Haavik et al. 2000; Glazyrin et al. 2012). The oxygen coordinates reported by Nakagiri
320 et al. (1986) and Gatta et al. (2007) are smaller than the values obtained in this study and
321 show a little decrease with pressure. Rozenberg et al. (2007) report oxygen coordinates that
322 first decrease slightly up to pressures of ~5 GPa, then show a strong increase with a maximum
323 around ~15 GPa, followed by a decrease up to 20 GPa. This behavior follows the same
324 pressure evolution previously discussed for the tetrahedral volumes, and is not confirmed by
325 the single-crystal data collected in this study nor by any other study on magnetite available in
326 literature (Finger et al. 1986; Nakagiri et al. 1986; Haavik et al. 2000; Gatta et al. 2007;
327 Glazyrin et al. 2012). Since the change in polyhedral volumes depend on a single coordinate
328 of the O atoms inside the crystal structure of magnetite, data collected on a powder sample are
329 often more difficult to analyze and more prone to misinterpretation. Rozenberg et al. (2007)
330 could have experienced problems due to data quality, resulting in biased values produced by
331 Rietveld refinements on their powdered magnetite sample. In particular, Glazyrin et al. (2012)
332 suggested that the peculiar trend reported from a powder sample analysis by Rozenberg et al.
333 (2007) could have originated from an insufficient number of diffracting crystallites potentially
334 a with strong grain size hysteresis as well as from texture evolution. Our single-crystal results
335 are consistent with the single-crystal structural refinements shown in Glazyrin et al. (2012),
336 and we consider that they resolve an important controversy.

337

338

Implications

339 Magnetite is commonly found as a stable phase in many geological contexts, however, until
340 now, its thermal equation of state (P - V - T relations) was not experimentally determined. The
341 mixed iron valence at the octahedral site makes magnetite also a challenge for calculations.

342 As such the here-obtained thermal EoS does not only greatly enhance current knowledge of
343 the thermo-elastic properties of magnetite, but it also adds the thermal EoS of a Fe³⁺-bearing
344 mineral to the available databases for self-consistent thermodynamic modeling (e.g., Stixrude
345 & Lithgow-Bertelloni 2011, Holland et al. 2013) and provides a critical benchmark to ab
346 initio approaches (e.g. Dorogokupets et al. 2016).

347 Recently magnetite was found to be a potentially important constituent of a phase
348 assemblages representative of the Martian upper mantle (Xu et al. 2021). Although present
349 only in a small amount, this experimental observation prompts for a reconsideration of the
350 importance of magnetite for our understanding of the Martian mantle and asks for including
351 magnetite in modeling the sound velocities and densities of a bulk assemblage representative
352 of Mars. Noteworthy, the effects of magnetite, or of Fe³⁺-bearing minerals more in general,
353 were not considered in any of the *a priori* velocity models used as guidance to the
354 interpretation of the Mars seismic records (Smrekar et al. 2019; Giardini et al. 2020; Stähler et
355 al. 2021) due to the absence of Fe³⁺ in end-member phases in the Stixrude and Lithgow-
356 Bertelloni (2011) database. The data collected in our study enables a more sophisticated
357 modeling of Mars' interior at least concerning the bulk sound velocity $v_{\Phi} = \sqrt{K/\rho}$, where K
358 corresponds to the bulk modulus and ρ to the density, respectively. Indeed, it allows
359 evaluating the contribution of magnetite to the seismic signal of the Martian upper mantle.

360 As a first example, we can consider the phase proportions proposed in Xu et al. (2021),
361 namely 50 vol% orthopyroxene, 44 vol% olivine and 6 vol% of magnetite, representative of a
362 Martian mantle mineralogy at a depth of ~250 km, versus a magnetite-free bulk rock
363 containing 53 vol% orthopyroxene and 47 vol% olivine. The orthopyroxene was modeled to
364 consist of 80 % enstatite (MgSiO₃) and 20 % ferrosilite (FeSiO₃) end-members and the
365 olivine of 77.5 % forsterite (Mg₂SiO₄) and 22.5 % fayalite (Fe₂SiO₄) end-members,
366 respectively (Xu et al. 2021). The change in bulk velocity was calculated using the finite

367 strain approach with the Debye-Mie-Grüneisen model and the elastic properties for
368 orthopyroxene and olivine reported by Stixrude and Lithgow-Bertelloni (2005, 2011) along a
369 representative areotherm for Mars established through 3-D thermal evolution models (case 12
370 by Plesa et al. (2018)). This specific areotherm assumes a relatively thin average crustal
371 thickness for Mars of 45 km, in agreement with recent findings by Knapmeyer-Endrun et al.
372 (2021) who argue for a crustal thickness less than 40 km below the InSight lander.
373 Generalization to different temperature profiles is straightforward. Figure 4 shows the bulk
374 velocity of both phase assemblages versus depth. An incorporation of 6 vol% magnetite in the
375 phase assemblage lowers the bulk velocity by ~12 m/s corresponding to ~0.21 % compared to
376 the magnetite-free bulk assemblage. Not surprisingly, magnetite being the minor phase in the
377 assemblages and having v_{Φ} very close to v_{Φ} of the modelled Martian assemblage (Figure S2),
378 the effect is quite small and is well below the current seismic detection limit of the InSight
379 mission on Mars. Nonetheless, our study improves the methodological approach, fully
380 contributing to the general understanding and providing a deeper insight with respect to the
381 previously uncharacterized effect of an Fe³⁺-rich mineral on the bulk velocities of a Martian
382 upper mantle. When considering the large diversity of possible chemical and mineralogical
383 compositions of rocky exoplanets (e.g. Putirka and Rarick 2019), any modeling omitting Fe³⁺-
384 rich minerals could result in an oversimplification, particularly in the case of planetary
385 environments having formed in relatively oxidizing conditions. In the case of Mars, Fe³⁺-
386 bearing phases such as magnetite are very important for mineralogical models since they bear
387 a signature for the redox state of Mars' mantle involving complex thermodynamic
388 equilibrium, even when their effects of seismic velocity are minor.

389

390

Acknowledgements

391 We thank the technical editor, Giovanni B. Andreozzi and one anonymous reviewer for their
392 constructive comments and G. Diego Gatta for handling the revision process of this
393 manuscript. We thank the Sorbonne University Mineral Collection for the provision of the
394 samples. The authors wish to thank Imène Estève for her help with sample analysis by SEM at
395 the Institut de Minéralogie de Physique des Matériaux et de Cosmochimie (IMPMC, Paris)
396 and Nicolas Rividi for his help during microprobe analysis at the Centre Camparis, Sorbonne
397 Université (Paris, France). Tainá Maciel, Ludovic Delbes, Benoît Baptiste and Eglantine
398 Boulard are acknowledged for preliminary measurements at the IMPMC X-ray diffraction
399 platform. This project has received funding from the European Research Council (ERC) under
400 the European Union's Horizon 2020 research and innovation Programme (Grant agreement
401 724690). This work was supported by the French Space Agency (CNES), focused on SEIS
402 instrument of the InSight mission. The Scanning Electron Microscope (SEM) facility at
403 IMPMC is supported by Région Ile de France grant SESAME 2006 N°I-07-593/R, INSU-
404 CNRS, Institute de Physique (INP)–CNRS, University Pierre et Marie Curie–Paris 6, and by
405 the French National Research Agency (ANR) grant ANR-07-BLAN-0124-01. This research
406 was carried out at the P02.2 Extreme Conditions Beamline at DESY, a member of the
407 Helmholtz Association (HGF). The research leading to this result has been supported by the
408 project CALIPSOplus under the Grant Agreement 730872 from the EU Framework
409 Programme for Research and Innovation HORIZON 2020. This paper is InSight contribution
410 261.

411

References

- 412 Angel, R.J., Bujak, M., Zhao, J., Gatta, G.D., and Jacobsen, S.D. (2007) Effective hydrostatic
413 limits of pressure media for high-pressure crystallographic studies. *Journal of Applied*
414 *Crystallography*, 40, 26–32.
- 415 Angel, R.J., Gonzalez-platas, J., and Alvaro, M. (2014) EosFit7c and a Fortran module (
416 library) for equation of state calculations, 229, 405–419.
- 417 Angel, R.J., Alvaro, M., Schmid-Beurmann, P., and Kroll, H. (2020) Commentary on
418 “Constraints on the Equations of State of stiff anisotropic minerals: rutile, and the
419 implications for rutile elastic barometry” [*Miner. Mag.* 83 (2019) pp. 339–347] .
420 *Mineralogical Magazine*, 84, 355–357.
- 421 Boehler, R., and De Hantsetters, K. (2004) New anvil designs in diamond-cells. *High Pressure*
422 *Research*, 24, 391-396.
- 423 Bruschini, E., Speziale, S., Andreozzi, G.B., Bosi, F., and Hålenius, U. (2015) The elasticity
424 of MgAl₂O₄-MnAl₂O₄ spinels by Brillouin scattering and an empirical approach for bulk
425 modulus prediction. *American Mineralogist*, 100, 644-651.
- 426 Dewaele, A., Loubeyre, P., and Mezouar, M. (2004) Equations of state of six metals above 94
427 GPa. *Physical Review B - Condensed Matter and Materials Physics*, 70, 1–8.
- 428 Ding, Y., Haskel, D., Ovchinnikov, S.G., Tseng, Y.C., Orlov, Y.S., Lang, J.C., and Mao, H.K.
429 (2008) Novel pressure-induced magnetic transition in magnetite (Fe₃O₄). *Physical*
430 *Review Letters*, 100, 18–21.
- 431 Dorogokupets, P.I., and Dewaele, A. (2007) Equations of state of MgO, Au, Pt, NaCl-B1, and
432 NaCl-B2: Internally consistent high-temperature pressure scales. *High Pressure*
433 *Research*, 27, 431–446.

- 434 Dorogokupets, P.I., Sokolova, T.S., Dymshits, A.M., and Litasov, K. D. (2016)
435 Thermodynamic properties of rock-forming oxides, α -Al₂O₃, Cr₂O₃, α -Fe₂O₃, and Fe₃O₄
436 at high temperatures and pressures. *Geodynamics and Tectonophysics*, 7, 459-476.
- 437 Fei, Y., Frost, D.J., Mao, H., Prewitt, C.T., and Hausermann, D. (1999) In situ structure
438 determination of the high-pressure phase of Fe₃O₄. *American Mineralogist*, 84, 203–
439 206.
- 440 Finger, L.W., Hazen, R.M., and Hofmeister, A.M. (1986) High-Pressure crystal chemistry of
441 spinel (MgAl₂O₄) and magnetite (Fe₃O₄): Comparisons with silicate spinels. *Physics
442 and Chemistry of Minerals*, 13, 215–220.
- 443 Gatta, G.D., Kantor, I., Boffa Ballaran, T., Dubrovinsky, L., and McCammon, C. (2007)
444 Effect of non-hydrostatic conditions on the elastic behaviour of magnetite: An in situ
445 single-crystal X-ray diffraction study. *Physics and Chemistry of Minerals*, 34, 627–635.
- 446 Giardini, D., Lognonné, P., Banerdt, W. B., Pike, W. T., Christensen, U., Ceylan, S., Clinton,
447 M., van Driel, S., Stähler, S., Böse, M., and others (2020). The seismicity of Mars.
448 *Nature Geoscience*, 13(3), 205–212.
- 449 Glazyrin, K., McCammon, C., Dubrovinsky, L., Merlini, M., Schollenbruch, K., Woodland,
450 A., and Hanfland, M. (2012) Effect of high pressure on the crystal structure and
451 electronic properties of magnetite below 25 GPa. *American Mineralogist*, 97, 128–133.
- 452 Glazyrin, K., Miyajima, N., Smith, J.S., and Lee, K.K.M. (2016) Compression of a
453 multiphase mantle assemblage: Effects of undesirable stress and stress annealing on the
454 iron spin state crossover in ferropicriase. *Journal of Geophysical Research: Solid Earth*,
455 121, 3377-3392.
- 456 Gonzalez-Platas, J., Alvaro, M., Nestola, F., and Angel, R. (2016) EosFit7-GUI: A new
457 graphical user interface for equation of state calculations, analyses and teaching. *Journal*

- 458 of Applied Crystallography, 49, 1377–1382.
- 459 Haavik, C., Stølen, S., Fjellvåg, H., Hanfland, M., and Häusermann, D. (2000) Equation of
460 state of magnetite and its high-pressure modification: Thermodynamics of the Fe-O
461 system at high pressure. American Mineralogist, 85, 514–523.
- 462 Holland, T. J.B., Hudson, N. F. C., Powell, R., and Harte, B. (2013) New thermodynamic
463 models and calculated phase equilibria in NCFMAS for basic and ultrabasic
464 compositions through the transition zone into the uppermost lower mantle. Journal of
465 Petrology, 54(9), 1901–1920.
- 466 Huang, E., and Bassett, W.A. (1986) Rapid Determination of Fe₃O₄ Phase Diagram by
467 Synchrotron Radiation. Journal of Geophysical Research, 91, 4697–4703.
- 468 Hübschle, C.B., Sheldrick, G.M., and Dittrich, B. (2011) ShelXle: A Qt graphical user
469 interface for SHELXL. Journal of Applied Crystallography, 44, 1281–1284.
- 470 Khandarkhaeva, S., Fedotenko, T., Chariton, S., Bykova, E., Ovsyannikov, S.V., Glazyrin, K.,
471 Liermann, H.-P., Prakapenka, V., Dubrovinskaia, N., and Dubrovinsky, L. (2022)
472 Structural Diversity of Magnetite and Products of its Decomposition at Extreme
473 Conditions. Inorganic Chemistry, 61, 1091-1101.
- 474 Klotz, S., Chervin, J.C., Munsch, P., and Le Marchand, G. (2009) Hydrostatic limits of 11
475 pressure transmitting media. Journal of Physics D: Applied Physics, 42.
- 476 Knapmeyer-Endrun, B., Panning, M.P., Bissig, F., Joshi, R., Khan, A., Kim, D., Lekić, V.,
477 Tauzin, B., Tharimena, S., Plasman, M., and others (2021) Thickness and structure of the
478 martian crust from InSight seismic data. Science, 373, 438–443.
- 479 Kouvel, J.S. (1956) Specific Heat of a Magnetite Crystal at Liquid Helium Temperatures,
480 106, 1489–1490.

- 481 Kuriki, A., Moritomo, Y., Ohishi, Y., Kato, K., Nishibori, E., Takata, M., Sakata, M.,
482 Hamada, N., Todo, S., Mori, N., and others (2002) High-Pressure Structural Analysis of
483 Fe₃O₄. *Journal of the Physical Society of Japan*, 71, 3092–3093.
- 484 Larson, A.C., and Von Dreele, R.B. (2004) General structure analysis system (GSAS). Los
485 Alamos National Laboratory Report, Report, 86–748.
- 486 Lazor, P., Shebanova, O.N., and Annersten, H. (2004) High-pressure study of stability of
487 magnetite by thermodynamic analysis and synchrotron X-ray diffraction. *Journal of*
488 *Geophysical Research: Solid Earth*, 109, 1–16.
- 489 Liermann, H.P., Konôpková, Z., Morgenroth, W., Glazyrin, K., Bednarčík, J., McBride, E.E.,
490 Petitgirard, S., Delitz, J.T., Wendt, M., Bican, Y., and others (2015) The Extreme
491 Conditions Beamline P02.2 and the Extreme Conditions Science Infrastructure at
492 PETRA III. *Journal of Synchrotron Radiation*, 22, 908–924.
- 493 Mao, H.-K., Takahashi, T., Bassett, W.A., Kinsland, G.L., and Merrill, L. (1974) Isothermal
494 compression of magnetite to 320 KB. *Journal of Geophysical Research*, 79, 1165–1170.
- 495 Nakagiri, N., Manghnani, M.H., Ming, L.C., and Kimura, S. (1986) Nakagiri et al.1986.pdf.
496 *Physics and Chemistry of Minerals*, 13, 238–244.
- 497 Otto, J., Vassiliou, J., and Frommeyer, G. (1998) Nonhydrostatic compression of elastically
498 anisotropic polycrystals. II. Direct compression and plastic deformation. *Physical*
499 *Review B - Condensed Matter and Materials Physics*, 57, 3264–3272.
- 500 Pasternak, M.P., Xu, W.M., Rozenberg, G.K., Taylor, R.D., and Jeanloz, R. (2003) Pressure-
501 induced coordination crossover in magnetite; the breakdown of the Verwey-Mott
502 localization hypothesis. *Journal of Magnetism and Magnetic Materials*, 265, 107–112.
- 503 Piermarini, G.J., Block, S., and Barnett, J.D. (1973) Hydrostatic limits in liquids and solids to

- 504 100 kbar. *Journal of Applied Physics*, 44, 5377–5382.
- 505 Plesa, A.C., Padovan, S., Tosi, N., Breuer, D., Grott, M., Wieczorek, M.A., Spohn, T.,
506 Smrekar, S.E., and Banerdt, W.B. (2018) The Thermal State and Interior Structure of
507 Mars. *Geophysical Research Letters*, 45, 12,198-12,209.
- 508 Prescher, C., and Prakapenka, V.B. (2015) DIOPTAS: a program for reduction of two-
509 dimensional X-ray diffraction data and data exploration. *High Pressure Research*, 35:3,
510 223-230.
- 511 Putirka, K.D., and Rarick, J.C. (2019) The composition and mineralogy of rocky exoplanets:
512 A survey of >4000 stars from the Hypatia Catalog. *American Mineralogist*, 104, 817-
513 829.
- 514 Rashchenko, S. V., Kurnosov, A., Dubrovinsky, L., and Litasov, K.D. (2015) Revised
515 calibration of the Sm:SmB₄O₇ pressure sensor using the Sm-doped yttrium-aluminum
516 garnet primary pressure scale. *Journal of Applied Physics*, 117, 2–7.
- 517 Reichmann, H.J., and Jacobsen, S.D. (2004) High-pressure elasticity of a natural magnetite
518 crystal. *American Mineralogist*, 89, 1061–1066.
- 519 Rozenberg, G.K., Amiel, Y., Xu, W.M., Pasternak, M.P., Jeanloz, R., Hanfland, M., and
520 Taylor, R.D. (2007) Structural characterization of temperature- and pressure-induced
521 inverse normal spinel transformation in magnetite. *Physical Review B - Condensed
522 Matter and Materials Physics*, 75, 2–5.
- 523 Scheidl, K.S., Kurnosov, A., Trots, D.M., Boffa Ballaran, T., Angel, R.J., and Miletich, R.
524 (2016) Extending the single-crystal quartz pressure gauge up to hydrostatic pressure of
525 19 GPa. *Journal of Applied Crystallography*, 49, 2129-2137.
- 526 Sheldrick, G.M. (2015) Crystal structure refinement with SHELXL. *Acta Crystallographica*

- 527 Section C: Structural Chemistry, 71, 3–8.
- 528 Smrekar, S. E., Lognonné, P., Spohn, T., Banerdt, W. B., Breuer, D., Christensen, U., Dehant,
529 V., Drilleau, M., Folkner, W., Fuji, N., and others (2019). Pre-mission InSights on the
530 Interior of Mars. *Space Science Reviews*, 215, 1–72.
- 531 Stähler, S.C., Khan, A., Banerdt, W.B., Lognonné, P., Giardini, D., Ceylan, S., Drilleau, M.,
532 Duran, A.C., Garcia, R.F., Huang, Q., and others (2021) Seismic detection of the martian
533 core. *Science*, 373, 443-448.
- 534 Stixrude, L., and Lithgow-Bertelloni, C. (2005) Thermodynamics of mantle minerals - I.
535 Physical properties. *Geophysical Journal International*, 162, 610–632.
- 536 Stixrude, L., and Lithgow-Bertelloni, C.(2011) Thermodynamics of mantle minerals - II.
537 Phase equilibria. *Geophysical Journal International*, 184, 1180–1213.
- 538 Tao, R., Fei, Y., Bullock, E.S., Xu, C., and Zhang, L. (2018) Experimental investigation of
539 Fe³⁺-rich majoritic garnet and its effect on majorite geobarometer. *Geochimica et*
540 *Cosmochimica Acta*, 225, 1–16.
- 541 Toby, B.H. (2001) EXPGUI, a graphical user interface for GSAS. *Journal of Applied*
542 *Crystallography*, 34, 210–213.
- 543 Verwey, E.J.W. (1939) Electronic Conduction of Magnetite (Fe₃O₄) and its Transition Point
544 at Low Temperatures. *Nature*, 144, 327–328.
- 545 Xu, F., Siersch, N.C., Gréaux, S., Rivoldini, A., Kuwahara, H., Kondo, N., Wehr, N.,
546 Menguy, N., Kono, Y., Higo, Y., and others (2021) Low Velocity Zones in the Martian
547 Upper Mantle Highlighted by Sound Velocity Measurements. *Geophysical Research*
548 *Letters*, 48, 1–8.
- 549

550

Figure captions

551 **Figure 1:** a) Pressure evolution of the unit-cell volume of magnetite at 300 K. Values
552 obtained in this study, normalized with respect to the room pressure measurement, (black
553 open and closed symbols) are compared to literature data (colored symbols). Data obtained
554 from powder X-ray diffraction (Mao et al. 1974; Nakagiri et al. 1986; Haavik et al. 2000;
555 Kuriki et al. 2002; Lazor et al. 2004; Rozenberg et al. 2007; this study) are shown as open
556 symbols and single-crystal data (Finger et al. 1986; Reichmann and Jacobsen 2004; Gatta et
557 al. 2007; Glazyrin et al. 2012; this study) are plotted as closed symbols. b) High-pressure and
558 high-temperature volume of Fe₃O₄ magnetite obtained in this study. High-temperature data
559 collected upon heating to 1100 K are shown as color-coded circles for increasing temperature:
560 red = 574(50) K, rose = 687(50) K, purple = 772(57) K, blue = 874(68) K, light blue =
561 977(63) K, green = 1075(65) K. Lines across experimental points are the outcome of fitting to
562 a BM2 EoS combined with a Mie-Grüneisen-Debye (MGD) model for the thermal pressure
563 (see text for details).

564

565 **Figure 2:** a) Pressure evolution of the volume of the octahedral (V_{oct}) and tetrahedral (V_{tet})
566 sites measured in this study (black symbols) and literature data (colored symbols, Finger et al.
567 1986; Haavik et al. 2000; Gatta et al. 2007; Rozenberg et al. 2007; Glazyrin et al. 2012). b)
568 Polyhedral volumes measured in this study at high pressure and high temperature. Data
569 collected upon heating follows the same color code as reported in Figure 1b.

570

571 **Figure 3:** Comparison of the evolution of the oxygen fractional coordinate u with increasing
572 pressure obtained using data collected in this study (both room temperature and high-
573 temperature) and reported in the literature (Finger et al. 1986; Nakagiri et al. 1986; Haavik et
574 al. 2000; Gatta et al. 2007; Rozenberg et al. 2007; Glazyrin et al. 2012). The dashed line is a

575 guide to the eye showing the evolution of u with pressure at ambient temperature observed in
576 this study.

577

578 **Figure 4:** Bulk velocity v_ϕ versus depth calculated along areotherm case 12 proposed for
579 Mars (Plesa et al. 2018) for two phase assemblages: i) 50 % orthopyroxene, 44 % olivine and
580 6 % magnetite (black) and ii) magnetite-free bulk assemblage made by 53 % orthopyroxene
581 and 47 % olivine (red).

582

583

584

Tables

585 **Table 1:** Major element composition of the natural magnetite investigated in this study reported in oxides (wt%) and atoms per formula unit (apfu)
586 normalized to 4 oxygens.

| oxides | wt% | cations | apfu |
|----------------------------------|-----------|---------|----------|
| Na ₂ O | 0.01(2) | Na | 0.001(1) |
| CaO | 0.01(3) | Ca | 0.001(1) |
| MgO | 0.05(2) | Mg | 0.003(1) |
| MnO | 0.05(4) | Mn | 0.002(1) |
| FeO* | 30.66(27) | Fe | 2.985(6) |
| Fe ₂ O ₃ * | 68.15(59) | | |
| Al ₂ O ₃ | 0.10(3) | Al | 0.005(1) |
| Cr ₂ O ₃ | 0.07(2) | Cr | 0.002(1) |
| TiO ₂ | 0.07(4) | Ti | 0.002(1) |
| SiO ₂ | 0.01(3) | Si | 0.001(1) |
| Total | 99.18(81) | | 4.004(6) |

587

*initially measured as FeO and converted to FeO and Fe₂O₃ by assuming Fe³⁺/Fe_{tot} = 0.67

588 **Table 2:** *Unit-cell volumes of magnetite measured at listed pressures and temperatures. For*
 589 *the high-temperature datasets, the average of the two thermocouple readings was assumed as*
 590 *the sample's temperature and the standard deviation were taken as uncertainties. The*
 591 *pressure uncertainties were determined by the half difference between the measurements of*
 592 *the pressure standards taken before and after each XRD measurement.*

593

| <i>P</i> (GPa) | <i>T</i> (K) | <i>V</i> Å ³ |
|--------------------|--------------|-------------------------|
| <i>DAC_300Kpwd</i> | | |
| 0.0001(1) | 298 | 592.45(17) |
| 0.41(1) | 298 | 591.22(23) |
| 0.99(1) | 298 | 589.56(25) |
| 1.82(1) | 298 | 585.78(21) |
| 2.76(1) | 298 | 583.99(25) |
| 3.45(1) | 298 | 581.87(12) |
| 4.28(3) | 298 | 579.37(16) |
| 5.10(1) | 298 | 577.32(19) |
| 6.06(1) | 298 | 574.52(16) |
| 7.42(11) | 298 | 570.46(14) |
| 7.87(1) | 298 | 568.97(21) |
| 8.89(1) | 298 | 566.30(25) |
| 10.02(3) | 298 | 562.98(22) |
| 11.04(1) | 298 | 560.55(28) |
| 11.66(61) | 298 | 558.63(39) |
| 12.78(1) | 298 | 557.11(19) |
| 13.12(1) | 298 | 556.12(23) |
| 14.14(1) | 298 | 553.86(14) |
| 14.87(6) | 298 | 552.57(14) |
| <i>DAC_300Ksc</i> | | |
| 0.0001(1) | 298 | 592.26(6) |

| | | |
|----------|-----|-----------|
| 0.77(1) | 298 | 590.04(6) |
| 1.65(1) | 298 | 587.07(8) |
| 3.00(3) | 298 | 583.82(8) |
| 3.97(8) | 298 | 579.41(8) |
| 5.69(6) | 298 | 574.58(8) |
| 6.69(14) | 298 | 572.20(6) |
| 7.66(9) | 298 | 570.05(8) |
| 8.71(9) | 298 | 567.60(8) |
| 9.89(1) | 298 | 563.42(8) |
| 10.99(6) | 298 | 561.01(6) |
| 12.02(6) | 298 | 559.68(6) |
| 13.21(1) | 298 | 555.82(6) |
| 14.40(1) | 298 | 553.65(8) |
| 15.74(3) | 298 | 550.27(5) |

DAC_600K

| | | |
|-----------|---------|------------|
| 1.11(1) | 298 | 589.77(8) |
| 1.77(1) | 601(50) | 591.86(8) |
| 2.47(1) | 601(50) | 589.45(8) |
| 3.73(1) | 603(50) | 585.58(8) |
| 4.09(1) | 604(50) | 583.50(8) |
| 5.62(8) | 604(50) | 580.39(8) |
| 6.90(16) | 602(50) | 576.45(10) |
| 7.54(1) | 601(50) | 575.08(10) |
| 8.85(8) | 600(50) | 570.82(10) |
| 9.38(4) | 600(50) | 569.97(14) |
| 11.43(8) | 598(50) | 564.50(16) |
| 12.49(12) | 597(50) | 561.52(18) |
| 12.99(4) | 598(50) | 560.98(10) |

DAC_900K

| | | |
|---------|---------|------------|
| 3.61(1) | 883(59) | 593.23(22) |
|---------|---------|------------|

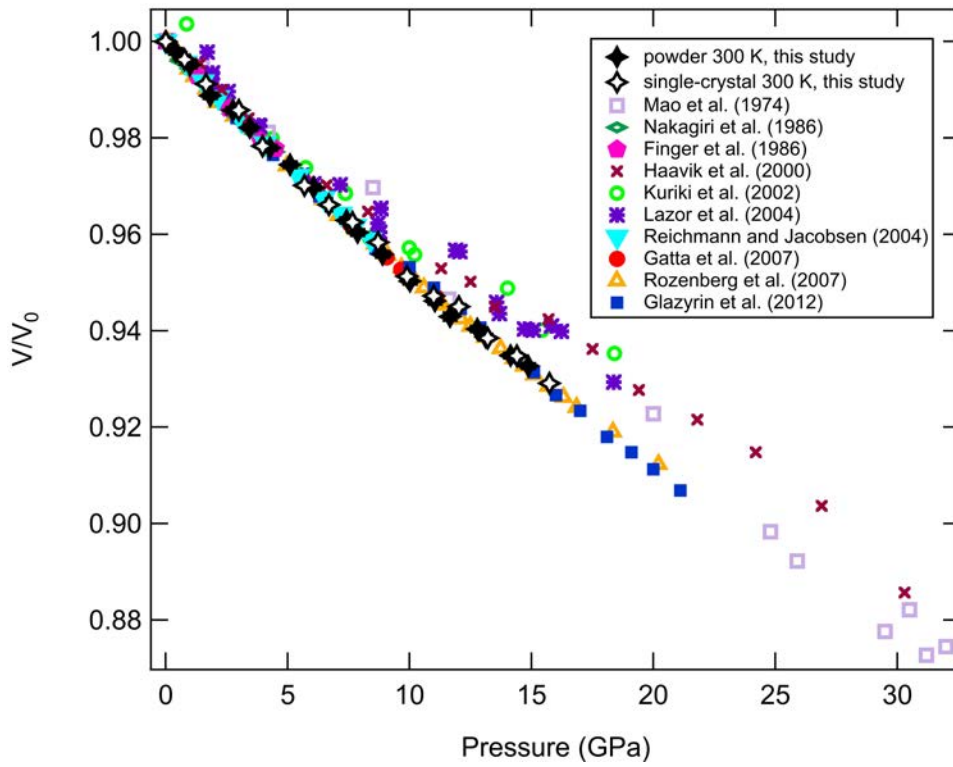
| | | |
|----------|---------|------------|
| 5.06(1) | 858(57) | 586.92(16) |
| 6.00(1) | 873(57) | 586.30(11) |
| 7.04(1) | 872(57) | 583.43(8) |
| 7.98(1) | 866(57) | 580.26(8) |
| 9.02(1) | 867(57) | 578.04(47) |
| 9.74(1) | 866(56) | 575.94(11) |
| 10.97(1) | 869(57) | 570.63(24) |
| 12.33(1) | 869(56) | 568.09(19) |
| 13.50(1) | 867(56) | 564.89(18) |

DAC_1100K

| | | |
|----------|----------|------------|
| 1.75(1) | 574(50) | 591.67(4) |
| 2.29(1) | 687(50) | 592.33(4) |
| 2.84(1) | 772(57) | 592.60(5) |
| 3.40(1) | 874(68) | 593.16(5) |
| 3.91(1) | 977(63) | 593.91(6) |
| 4.33(1) | 1075(65) | 594.60(6) |
| 4.82(1) | 1072(66) | 592.85(5) |
| 5.59(1) | 1060(67) | 590.51(4) |
| 6.27(1) | 1069(70) | 589.96(6) |
| 6.64(1) | 1064(70) | 586.96(5) |
| 7.34(1) | 1078(72) | 586.10(6) |
| 7.93(1) | 1071(72) | 583.10(6) |
| 8.27(1) | 1068(72) | 583.16(7) |
| 8.82(1) | 1062(72) | 580.43(7) |
| 9.58(1) | 1072(74) | 579.41(9) |
| 10.39(1) | 1065(75) | 575.86(13) |

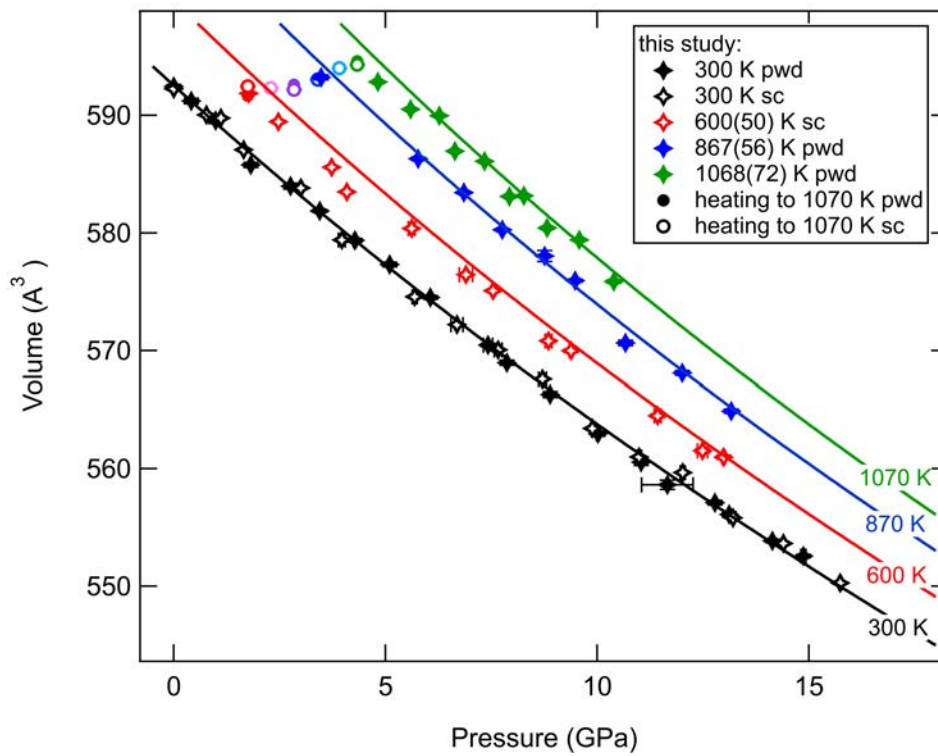
595 **Figures**

596 **Figure 1a**



597

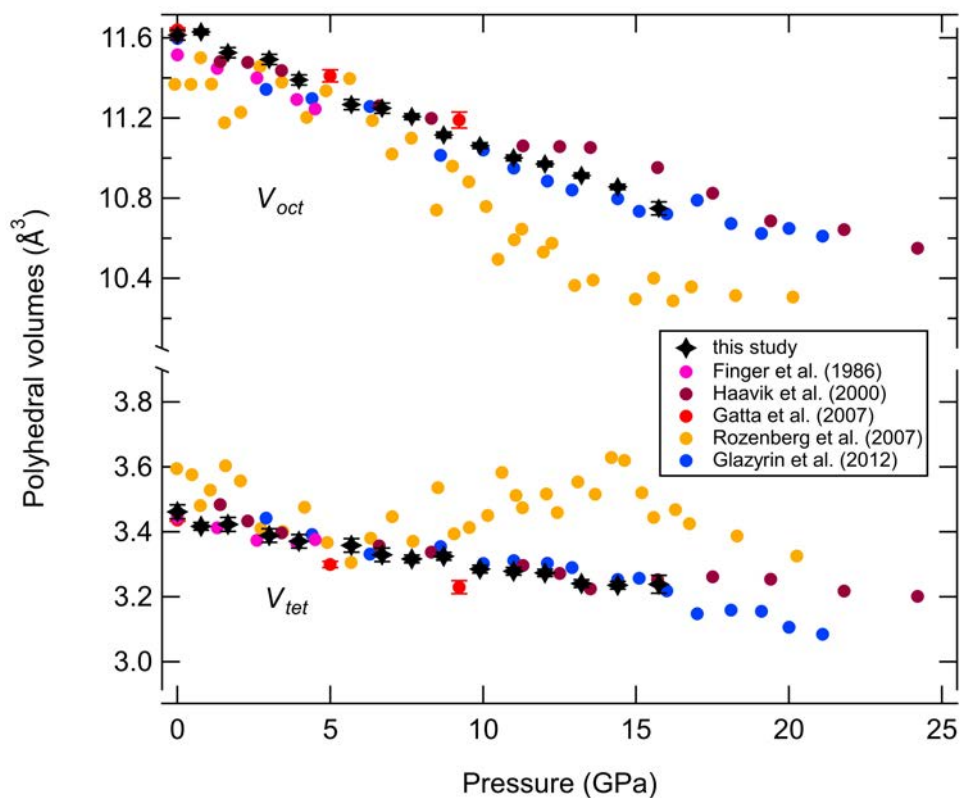
598 **Figure 1b**



599

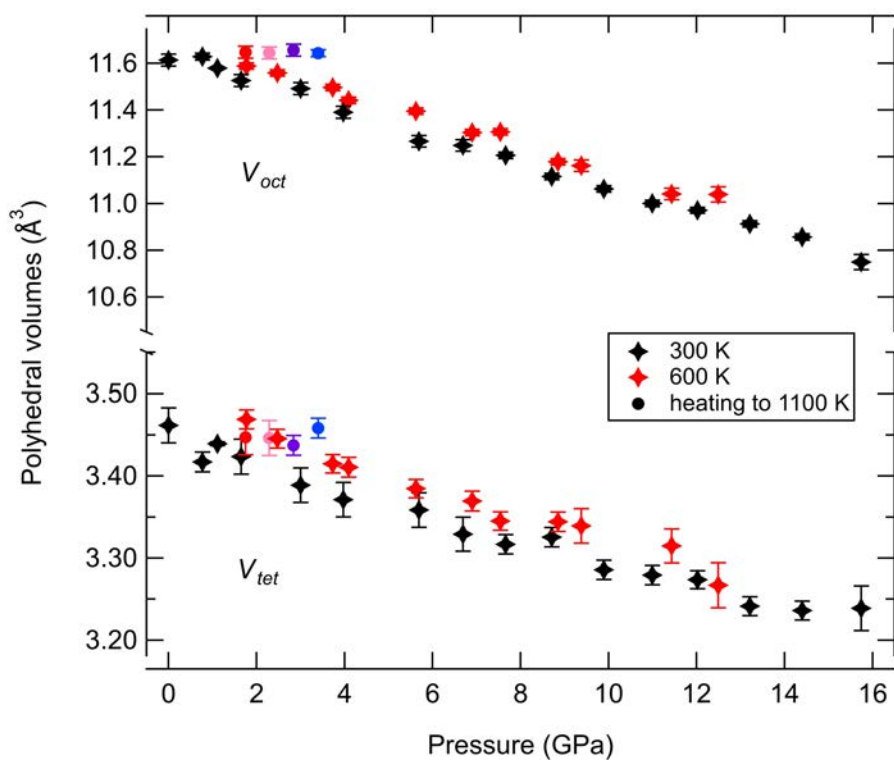
30

600 **Figure 2a**



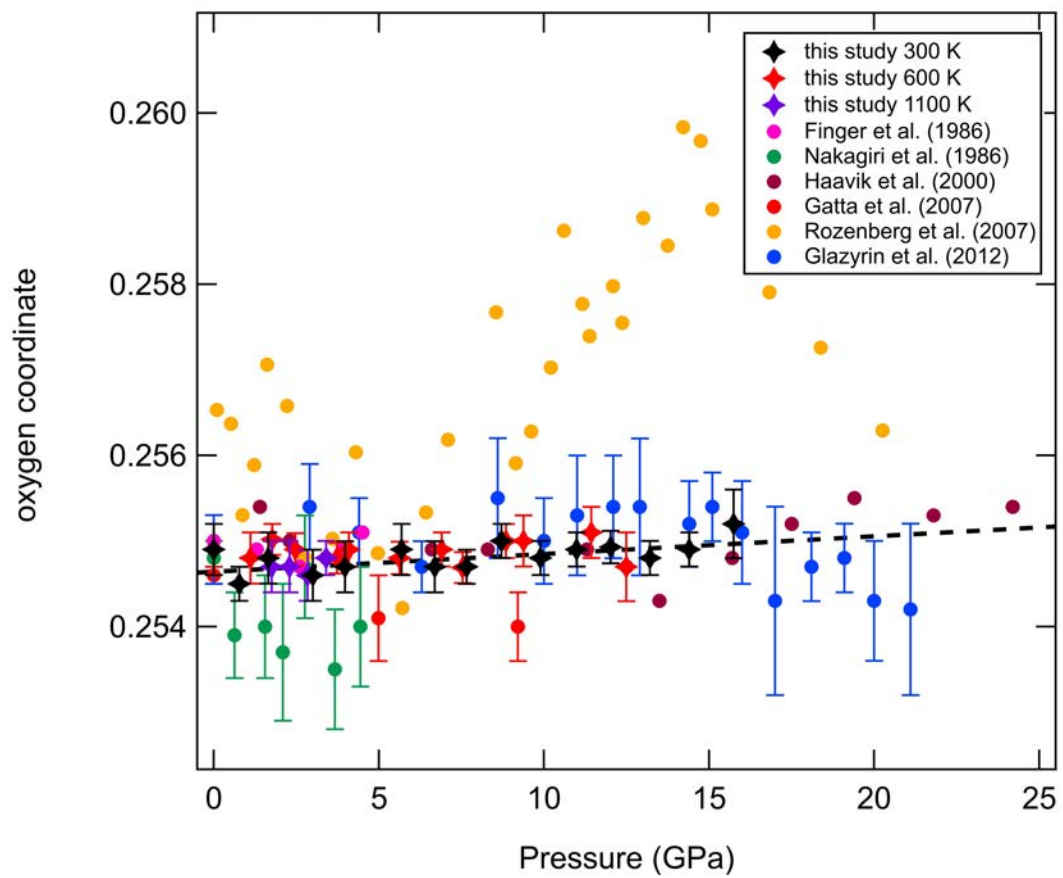
601

602 **Figure 2b**



603

604 **Figure 3**



605

606

607

608

609

610

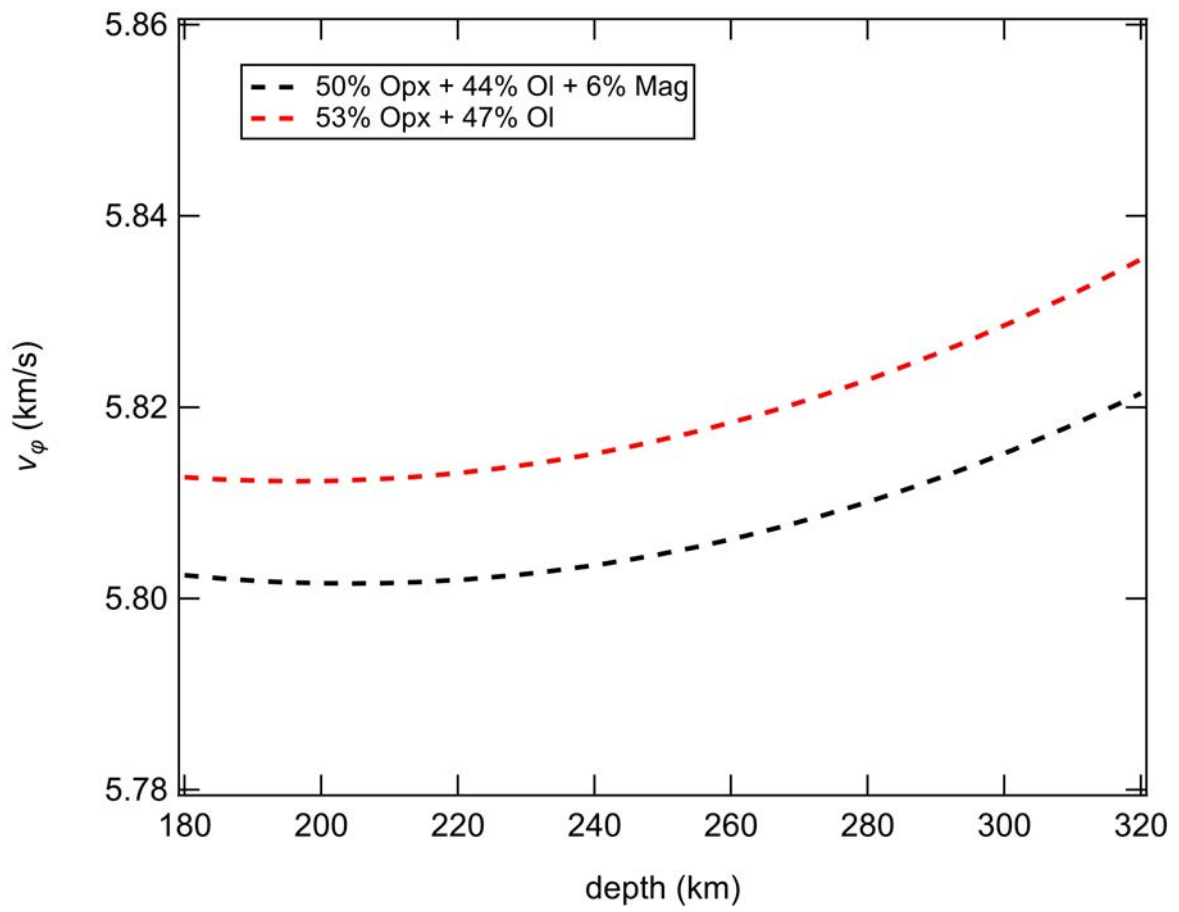
611

612

613

614 **Figure 4**

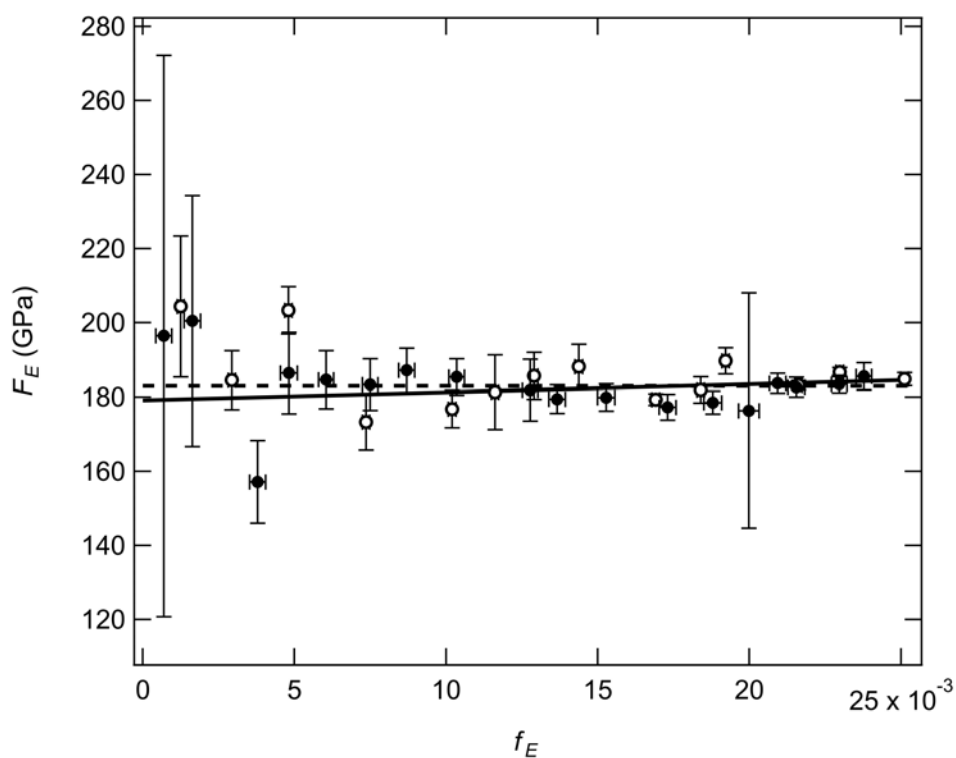
615



616

617 **Supplementary Information**

618 **Figure S1**



619

620 **Figure S1:** Normalized pressure (F_E) plotted against the Eulerian strain (f_E) for Fe_3O_4
621 magnetite measured at ambient temperature. The solid circles indicate data collected on a
622 powdered magnetite sample whereas the open circles indicate data obtained from a single-
623 crystal of magnetite. The lines represent 2nd (dashed) and 3rd (solid) order Birch-Murnaghan
624 fits through the dataset.

625

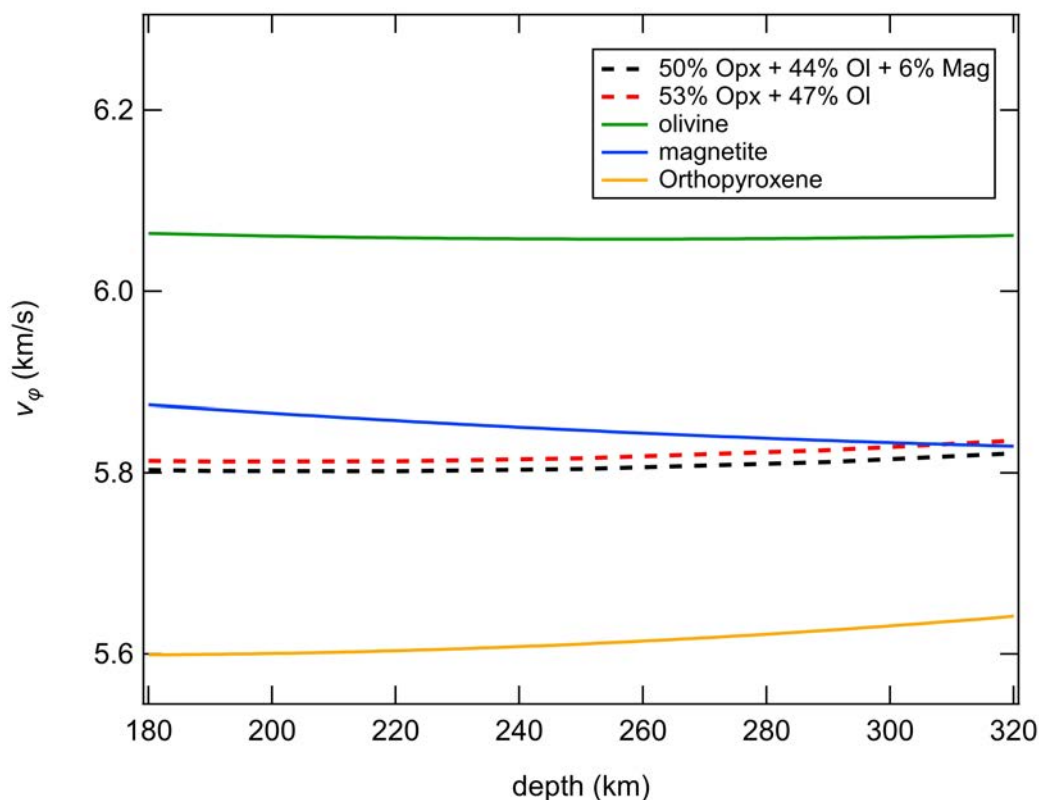
626

627

628

629

630 **Figure S2**



631

632 **Figure S2:** Bulk sound velocity v_ϕ calculated versus depth along areotherm case 12 proposed
633 for Mars (Plesa et al. 2018) for olivine (Fo77.5, green), magnetite (blue) and orthopyroxene
634 (En80, orange). These bulk velocities are compared to the two phase assemblages 1)
635 containing 50 % orthopyroxene, 44 % olivine and 6 % magnetite (black) and 2) a magnetite-
636 free bulk assemblage with 53 % orthopyroxene and 47 % olivine (red) as shown in Figure 4.

637

638

639

640

641

642

643 **Table S1:** Single-crystal unit-cell volumes of magnetite measured at different pressures and
 644 temperatures, oxygen coordinate u , R_{int} and RI and the number of unique reflections obtained
 645 in the structural refinements.

646

| P (GPa) | T (K) | V (Å ³) | u (-) | R_{int} (%) | RI (%) | No. Unique reflections |
|-------------------|---------|-----------------------|------------|---------------|----------|------------------------|
| <i>DAC_300Ksc</i> | | | | | | |
| 0.0001(1) | 298 | 592.26(6) | 0.2549(3) | 3.59 | 2.44 | 28 |
| 0.77(1) | 298 | 590.04(6) | 0.2545(2) | 3.14 | 2.28 | 29 |
| 1.65(1) | 298 | 587.07(8) | 0.2548(3) | 3.61 | 2.63 | 30 |
| 3.00(3) | 298 | 583.82(8) | 0.2546(3) | 2.59 | 2.70 | 30 |
| 3.97(8) | 298 | 579.41(8) | 0.2547(3) | 2.76 | 2.70 | 30 |
| 5.69(6) | 298 | 574.58(8) | 0.2549(3) | 3.19 | 2.43 | 28 |
| 6.69(14) | 298 | 572.20(6) | 0.2547(3) | 4.20 | 2.29 | 27 |
| 7.66(9) | 298 | 570.05(8) | 0.2547(2) | 2.38 | 2.41 | 27 |
| 8.71(9) | 298 | 567.60(8) | 0.2550(2) | 2.71 | 1.93 | 26 |
| 9.89(1) | 298 | 563.42(8) | 0.2548(2) | 3.34 | 2.38 | 27 |
| 10.99(6) | 298 | 561.01(6) | 0.2549(2) | 4.66 | 2.62 | 27 |
| 12.02(6) | 298 | 559.68(6) | 0.25493(2) | 2.67 | 1.79 | 27 |
| 13.21(1) | 298 | 555.82(6) | 0.2548(2) | 2.43 | 2.70 | 29 |
| 14.40(1) | 298 | 553.65(8) | 0.2549(2) | 2.58 | 2.27 | 27 |
| 15.74(3) | 298 | 550.27(5) | 0.2552(4) | 3.18 | 2.49 | 28 |
| <i>DAC_600K</i> | | | | | | |
| 1.11(1) | 298 | 589.77(8) | 0.2548(3) | 1.82 | 1.80 | 38 |

| | | | | | | |
|-----------|---------|------------|-----------|------|------|----|
| 1.77(1) | 601(50) | 591.86(8) | 0.2550(2) | 2.40 | 1.83 | 37 |
| 2.47(1) | 601(50) | 589.45(8) | 0.2549(2) | 2.99 | 1.77 | 37 |
| 3.73(1) | 603(50) | 585.58(8) | 0.2548(2) | 2.07 | 1.62 | 38 |
| 4.09(1) | 604(50) | 583.50(8) | 0.2549(2) | 2.41 | 1.56 | 37 |
| 5.62(8) | 604(50) | 580.39(8) | 0.2548(2) | 1.60 | 1.44 | 37 |
| 6.90(16) | 602(50) | 576.45(10) | 0.2549(2) | 1.98 | 1.94 | 36 |
| 7.54(1) | 601(50) | 575.08(10) | 0.2547(2) | 2.14 | 2.16 | 39 |
| 8.85(8) | 600(50) | 570.82(10) | 0.2550(2) | 3.07 | 2.46 | 34 |
| 9.38(4) | 600(50) | 569.97(14) | 0.2550(3) | 2.79 | 2.60 | 34 |
| 11.43(8) | 598(50) | 564.50(16) | 0.2551(3) | 2.76 | 2.22 | 35 |
| 12.49(12) | 597(50) | 561.52(18) | 0.2547(4) | 4.54 | 2.77 | 33 |

DAC_1100K

| | | | | | | |
|---------|---------|-----------|-----------|------|------|----|
| 1.75(1) | 574(50) | 592.47(6) | 0.2547(3) | 4.13 | 3.85 | 29 |
| 2.29(1) | 687(50) | 592.32(6) | 0.2547(3) | 3.80 | 3.59 | 33 |
| 2.84(1) | 772(57) | 592.17(6) | 0.2546(3) | 2.52 | 3.56 | 36 |
| 3.40(1) | 874(68) | 593.04(6) | 0.2548(2) | 3.81 | 1.89 | 30 |

647

648